

Full Length Article

Metastable wetting model of electrospun mats with wrinkled fibers



Amit Rawal^{a,b,*}, Siddharth Shukla^a, Sumit Sharma^a, Danvendra Singh^a, Yi-Min Lin^b, Junli Hao^b, Gregory C. Rutledge^b, Lívía Vásárhelyi^c, Gábor Kozma^c, Akos Kukovecz^c, László Janovák^d

^a Department of Textile and Fibre Engineering, Indian Institute of Technology Delhi, Hauz Khas, New Delhi, India

^b Department of Chemical Engineering, Massachusetts Institute of Technology, Cambridge, MA 02139, United States

^c University of Szeged, Interdisciplinary Excellence Centre, Department of Applied and Environmental Chemistry, University of Szeged, Rerrich Béla tér 1., Szeged, Hungary

^d University of Szeged, Department of Physical Chemistry and Materials Science, H-6720, Rerrich Béla tér 1, Szeged, Hungary

ARTICLE INFO

Keywords:
Electrospun
Metastable
Wetting
Analytical model

ABSTRACT

Electrospun mats with targeted wettability are a way forward to diversify their mainstream applications and can facilitate in creating a platform for a remarkable set of properties. Limited control over the fiber morphology and surface chemistry, along with the complex architecture of electrospun mats, pose some of the key challenges for maneuvering the wettability. Herein, we present the design principles that underpin the key determinants responsible for a metastable state of a water droplet on electrospun mats possessing wrinkled surface topography. A 'first-of-its-kind' analytical model of apparent contact angle based on the modified Cassie-Baxter state has been proposed that accounts for the dual-scale roughness originating from fiber wrinkles and protuberances created by fiber-fiber contacts. Three-dimensional (3D) fiber and structural parameters obtained via X-ray microcomputed tomography (microCT) analysis served as key inputs for predictive modeling. The analytical model of the apparent advancing and receding contact angles has been validated with electrospun mats having well-defined orientation characteristics. In general, the theory and experiments are in reasonable agreement. Although similar magnitudes of static and advancing contact angles of water on surfaces of randomly and aligned electrospun mats have been experimentally observed, the receding contact angles differed significantly.

1. Introduction

Targeting the interaction of liquids with solid surfaces in a precise manner is a gateway to overcome some of the key challenges associated with biological and technological applications [1]. The contact angle that is formed at the interface of liquid, air, and solid quantifies the wettability of a solid surface to that liquid. Typically, two extreme wetting regimes have been hypothesized in the literature – 'Wenzel' [2] and 'Cassie-Baxter' (CB) [3] – to explain the hydrophilic and hydrophobic states. These wetting regimes are primarily governed by surface chemistry and the roughness of the solid surface. Central to these wetting regimes is the unique fabrication methods involved in creating hydrophobic surfaces from innate hydrophilic materials or vice-versa.

Electrospinning is a distinct method to prepare a three-dimensional (3D) porous material that can trap the air at the surface and bulk of the material, which eventually delays the infiltration of liquid in the

structure [4]. Through a combination of surface roughness and surface chemistry, a range of metastable to highly robust, superhydrophobic to superhydrophilic electrospun mats have been successfully developed [5–7]. In the seminal work, Tuteja *et al.* [8] highlighted the importance of surface roughness in the form of re-entrant curvature and successfully fabricated the metastable superoleophobic electrospun mats using oleophilic surfaces. The metastable state has been effectively and extensively used by Nature to avoid steep protrusions that are susceptible to damage, thereby successfully creating superhydrophobic surfaces. A lotus leaf is a classic example, which exploits a metastable superhydrophobic state to attain a self-cleaning surface, even though the waxes present on it are weakly hydrophilic [9,10]. The metastable condition based upon key determinants (roughness, fraction of solid in contact with the liquid, Young's contact angle) for regular structures such as posts, pillars, etc., have been established in the literature [11,12]. However, the underlying design principles pin-pointing the key

* Corresponding author.

E-mail address: arawal@iitd.ac.in (A. Rawal).

<https://doi.org/10.1016/j.apsusc.2021.149147>

Received 27 September 2020; Received in revised form 21 January 2021; Accepted 25 January 2021

Available online 30 January 2021

0169-4332/© 2021 Elsevier B.V. All rights reserved.

determinants responsible for a metastable state of a liquid droplet in (disordered) electrospun mats need to be explicitly defined. The very same property of metastability becomes even more important for electrospun mats with dual/multi-scalar roughness [13,14]. One of the possibilities to create dual/multi-scalar roughness is realized by wrinkles present on the surface of the fibers. In electrospinning, these wrinkles can plausibly originate due to the buckling of a cylindrical polymer shell as a result of the removal of solvent from the core. A variety of surface wrinkles can be tailored either by stretching the polymer jet or through the process of annealing [13].

The present work aims to investigate and predict the metastable state of the liquid in contact with the electrospun mats having wrinkled surface topography. Here, the solution of polystyrene has been chosen for producing electrospun fibers as it enables a wide range of length scales and surface topographies [13–15] besides extensive industrial applications [16]. Even the minor modifications in the wetting characteristics of polystyrene-based electrospun mats can significantly assist in growing tissues [17] or enhance fog collection for water harvesting applications [18]. Therefore, the predictive model has accounted for a key set of fiber and structural parameters that facilitate in modulating the wetting characteristics in a relatively precise manner. Accordingly, the 3D structure of the prepared electrospun mats has been deciphered using X-ray microcomputed tomography (microCT) analysis for obtaining various fiber and structural parameters. A comparison has been made between the predicted and experimental water contact angles in advancing and receding modes of two distinct electrospun mats comprising preferentially and randomly aligned fibers. To the best of the authors' knowledge, this is a first attempt to predict the apparent contact angles of electrospun mats comprising wrinkled fibers.

2. Materials and methods

2.1. Preparation of electrospun mats

In this research work, the randomly and preferentially aligned electrospun mats were prepared from a 30 wt% solution of polystyrene ($M_w \sim 350$ kg/mol) dissolved in N, N-dimethylformamide (DMF). Initially, the solution of 30 wt% polystyrene in DMF was prepared by stirring overnight for electrospinning. The polymer solution was collected in a 10 mL syringe (BD) and subsequently extruded through a Teflon tube to 1 mm-ID stainless steel needle (Upchurch Scientific) with the help of Harvard Apparatus 11 Syringe Pump at a flow rate of 2 mL/h. The capillary needle was then subjected to 10 kV of power supply (Gamma High Voltage Research, ES40P) that pointed downwards to a grounded roller collector. The roller collector was made up of a metal mesh with a length and diameter of 20 cm and 12 cm, respectively. The collector had a covering of non-stick Reynolds aluminum foil. During the electrospinning process, the cylinder was connected to a rotary motor

and placed 28 cm below the capillary needle. The system was placed in an insulated acrylic box at 30% relative humidity. The randomly and preferentially aligned electrospun mats were prepared by rotating the collector at 30 rpm (circumferential velocity of 0.19 m/s), and 850 rpm (circumferential velocity of 5.34 m/s), respectively. These electrospun mats were deposited on the collector for 30 min to obtain the dimensions of 360 mm \times 110 mm \times 0.07 mm. The prepared randomly and preferentially aligned electrospun mats are referred to herein as 'ES-A' and 'ES-B', respectively. Fig. 1 shows the scanning electron microscopy images of polystyrene-based electrospun mats. The mean fiber diameter in ES-A and ES-B is given in Table S1.

2.2. X-ray micro-computed tomography analysis

The morphological analysis of the electrospun mats was performed using the X-ray micro-computed tomography technique. Here, the electrospun sample with an area of 2 mm \times 1.5 mm was scanned on a sample stage in combination with an open filter assembly that allowed the closest permissible proximity of the X-ray source for maximizing the image resolution. X-rays having a source current of 750 μ A and a source voltage of 60 kV were focused using a tungsten target to attain an exposure time of 600 ms by rotating in the steps of 0.20° covering an angular range of 194°. With the aid of commercially available software methods - NRecon and DataViewer (SkyScan, Bruker, Belgium), the image data were reconstructed using 2100–2300 images with a pixel size of 0.8–1 μ m. The attributes of the scanned images were improved by employing beam hardening correction, defect pixel, and ring artefact reduction techniques.

Notably, the resolution of the obtained images was comparable to that of the dimensions of the constituent fibers of the electrospun samples, and accordingly, certain irregularities in the form of noise and binarization artefacts were evident [19]. These issues were overcome using an edge-preserving median filter to suppress the noise. Subsequently, binarization and despeckling of images were performed to prepare the final data set for further processing. The details of these techniques are given in our earlier work [20].

The porosity of the electrospun mats has been determined via an in-built pixel counting algorithm by selectively choosing a volume of interest (VOI) of 0.011 mm³ in commercially available software, CTAn® (Bruker, Belgium). The pore size distribution has also been analyzed using the extracted VOI of the porosity by combining distance transform and local thickness algorithms [20]. Initially, the medial axis network of pore space was obtained when each voxel was replaced with an intensity value based upon a distance transform algorithm. Subsequently, the local thickness algorithm was employed by locally fitting the largest spheres on the brightest voxels [20]. The proportion of the pore volume occupied by the spheres of predefined diameters was used to describe the pore size distribution. Similarly, the CTAn® has been used for

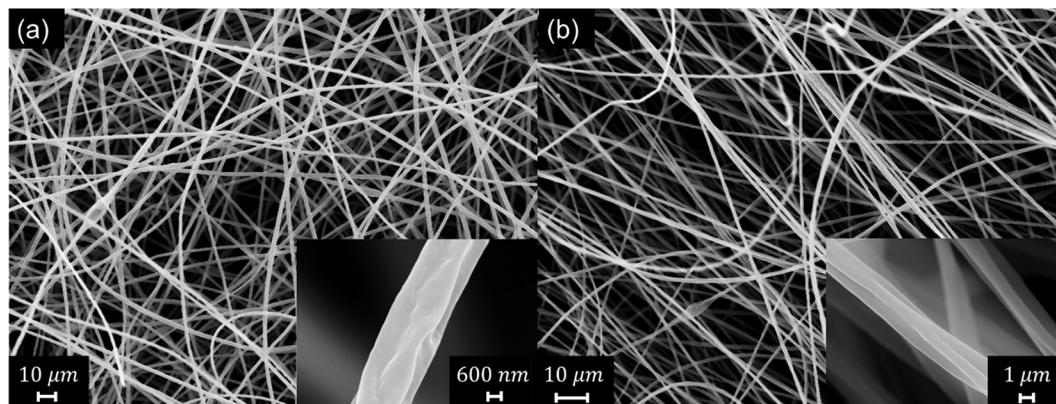


Fig. 1. Micrographs of (a) ES-A and (b) ES-B depicting the random and preferential alignment of fibers. The inset shows the morphology of constituent fibers.

analyzing the reconstructed images to obtain the fiber orientation distributions of the electrospun mats. The in-plane fiber orientation angle has been estimated by calculating the orientation of the major axis of the object (fiber) with the X-axis of the scanned images. On the other hand, the out-of-plane fiber orientation angle was determined by the main eigenvalues of the second moments of inertia of the objects. These fiber and structural parameters were used as a key set of inputs for predictive modeling of apparent contact angle.

2.3. Determination of water contact angle

The static apparent contact angles on the electrospun mats were measured by placing a 10 μL deionized water droplet using the KRUSS DSA-100 drop shape analyzer. Ten images of each of the samples were analyzed using ImageJ® software. The static contact angle of water on a smooth flat polystyrene surface was also measured and found to be 83° . Further, the dynamic contact angles were measured by a drop shape analyzer (KRUSS, Germany), which has a Peltier temperature chamber and a steel syringe needle of 0.5 mm. Initially, the drop volume was increased in steps using a syringe with a threaded plunger, which allows for more precise control over drop volume. Subsequently, the advancing contact angle was measured after injecting the water by increasing its volume to 15 μL . Receding contact angles were measured by withdrawing a fixed amount of water from the droplet in steps, and subsequently, the contact angle was measured after each volume reduction step. The experiments were repeated in three different positions for both electrospun mats.

2.4. Surface topography analysis

The surface topography of the electrospun samples was scanned and quantified using the tapping mode on an NT-MDT Solver Scanning Probe Microscope (NT-MDT Spectrum Instruments, Moscow, Russia) – a type of atomic force microscope (AFM). A detailed analysis of the scanned topography was performed using Gwyddion, an open-source program for the visualization and analysis of Scanning Probe Microscopy (SPM) data [21]. The surface topography obtained for the $12 \times 12 \mu\text{m}^2$ scan is shown in Fig. 2. The protrusions visible in the AFM plots belong to the constituent fibers present in the electrospun mat.

To determine the amplitude and wavelength of the wrinkle folds, the AFM data file was opened in the open-source software Gwyddion. Several crossing lines were drawn on the fiber, where the wrinkles were prominently visible. The surface profile data of the fiber along the lines were then extracted. Specifically, the surface profiles comprising wrinkles with well-defined peaks and valleys were obtained. The individual profiles were carved out separately by fitting a circle having a diameter as that of the constituent fiber in the electrospun mat. Subsequently, the values of amplitude and wavelength of the wrinkles were extracted from the protrusions lying on the surface of the fibers. The mean of the peaks was calculated, which was then averaged with the valley depth to obtain the value of the amplitude. The distance between the consecutive peaks along the curved fiber surface was calculated to obtain the magnitude of the wavelength. A step-wise approach for determining the amplitude and wavelength of the wrinkle surfaces is given in Figure S1 (see supplementary information).

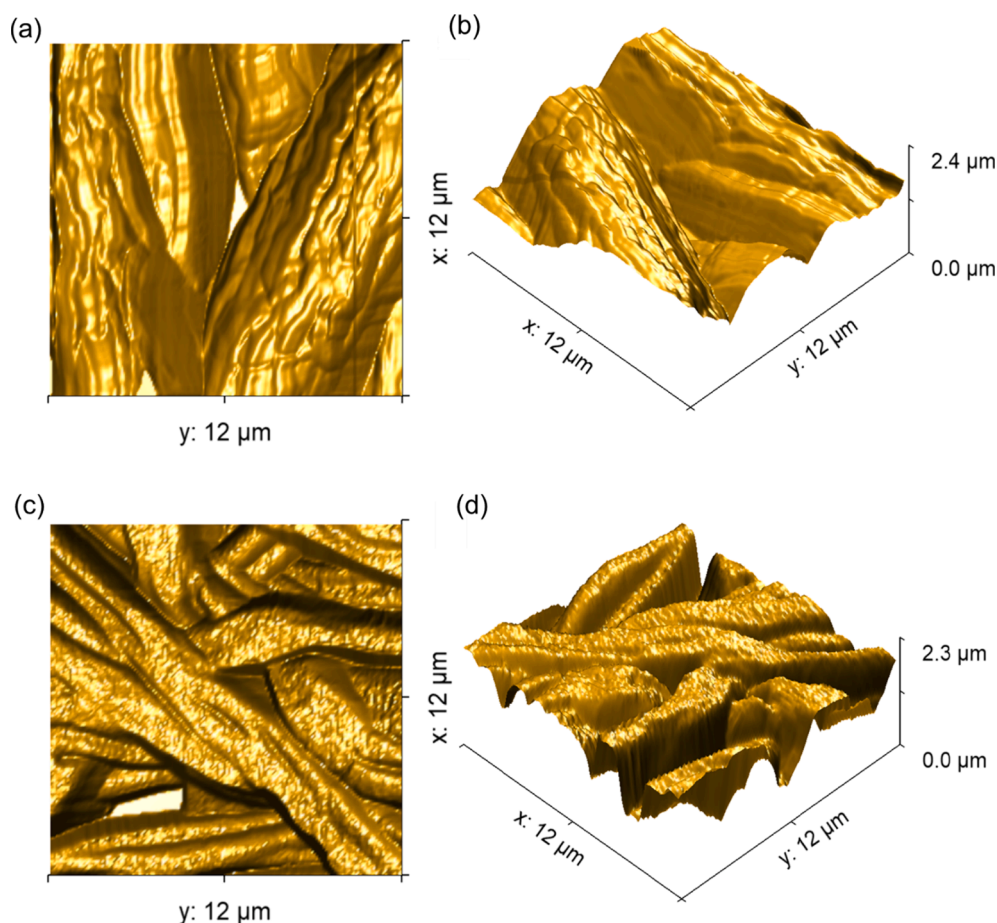


Fig. 2. AFM image analysis of electrospun mats (ES-A: a, b; ES-B: c, d). Here, the roughness is depicted in the planar view (a, c) and in the form of a 3D surface plot (b, d). The root mean square (RMS) roughness obtained for the ES-A and ES-B are found to be 414.29 and 439.26 nm, respectively.

3. Results and discussion

3.1. Structural analysis of electrospun mats

Fig. 3a and b depict the 3D rendered images of electrospun samples along with their fiber orientation distribution. As expected, a considerable proportion of in-plane fibers are aligned preferentially in the vicinity of the rotational direction ($70\text{--}90^\circ$) in ES-B, whereas the fibers in ES-A follow quasi-random characteristics (see Fig. 3c). As it is well known for electrospun mats, a majority of the fibers primarily lie in the XY plane, also demonstrated via out-of-plane fiber orientation distribution (see Fig. 3d). The ES-A is a relatively more planar structure in comparison to the ES-B. These results matched well with the previous research work [22] that also demonstrated the planar structure of the electrospun mats. To quantify the orientation characteristics of fibers, we computed the 3D orientation parameter (I) based upon the following equation [23],

$$I = \int_0^\pi d\beta \int_0^\pi J(\beta, \phi) \sin\beta \Omega(\beta, \phi) d\phi; \quad (1)$$

$$J(\beta, \phi) = \int_0^\pi d\gamma \int_0^\pi \sin\chi(\beta, \phi, \gamma, \zeta) \Omega(\gamma, \zeta) \sin\gamma d\zeta$$

$$\sin\chi(\beta, \phi, \gamma, \zeta) = [1 - \{\cos\beta\cos\gamma + \sin\beta\sin\gamma\cos(\phi - \zeta)\}^2]^{1/2}$$

where χ is the angle formed between the axes of two fibers with orientation distributions, i.e., $\Omega(\beta, \phi)$ and $\Omega(\gamma, \zeta)$, β, γ are the out-of-plane (polar) fiber orientation angles, and ϕ and ζ are the in-plane fiber (azimuthal) orientation angles according to the spherical co-ordinate system, respectively.

The value of I for a 3D structure is bounded between 0 (unidirectional) and $\pi/4$ (random). Table S1 shows that the magnitude of I is higher in the case of ES-A that corresponds to the randomness. A word of caution is needed here: a variety of fiber orientation distributions in the in-plane and out-of-plane directions can yield the same magnitude of I [24]. This is analogous to the Hermans orientation factor of 'zero' that

could either indicate the isotropic orientation of fibers or implies that all the fibers are aligned at 54.7° [25]. Therefore, the value obtained for the orientation parameter should be viewed cautiously. Nevertheless, the preferential alignment of fibers reduced the porosity of ES-B in comparison to ES-A, as depicted in Table S1. Accordingly, the narrow pore size distribution of ES-B was observed and compared to ES-A (see Figure S2).

3.2. Metastable state of liquid on wrinkled electrospun fibers

The pioneering work of Wenzel [2] by generalizing Young's equation for rough surfaces revealed the important concept of enhancing surface wettability via an increase in the contact area. The Wenzel state of the liquid invokes the thermodynamic arguments to explain the deviations in the apparent contact angle, as obtained from Young's equation [26], by assuming that the liquid follows the surface texture. The apparent contact angle of a homogenous rough surface (θ_W^*) was thus, predicted by introducing the roughness factor r - the ratio of the actual macroscopic area of a rough surface to that of a smooth surface with the same geometric shape and dimensions [2,27]. Therefore,

$$\cos\theta_W^* = r\cos\theta_Y \quad (2)$$

where θ_Y is the equilibrium contact angle determined on the smooth surface in accordance with Young's equation.

The roughness in an electrospun mat can be created by the surface topology of the fibers and also by the overlapping constituent fibers made via fiber-fiber contacts in a typical nonwoven mat [28]. Particularly, the roughness factor associated with the overlapping fibers (r_{el}) can be defined as the ratio of the actual surface area developed as a result of fiber-fiber contacts or overlapping fibers to that of a smooth surface in a typical representative volume element (RVE) [29]. Using the first principles of stereology and orientation average approaches, r_{el} can be obtained, as shown below [29]. Later, we will discuss the roughness created by the surface characteristics of fibers.

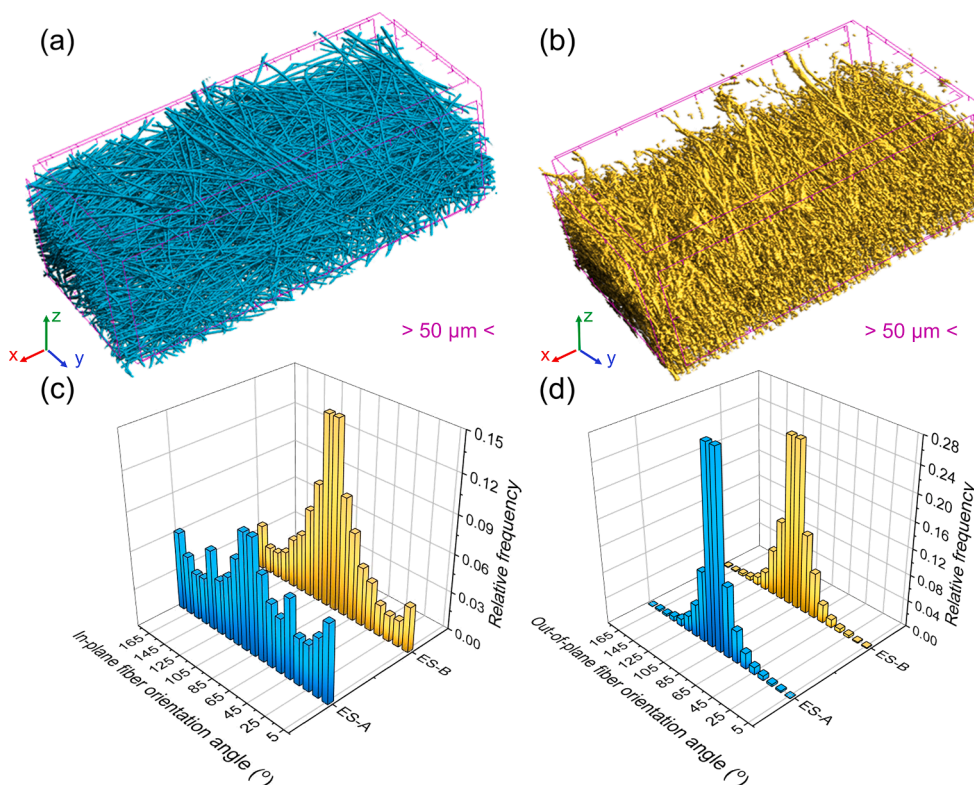


Fig. 3. Morphological analysis of electrospun samples performed via the X-ray micro-computed tomography technique. 3D rendered images of (a) ES-A and (b) ES-B presented along with their (c) in-plane and (d) out-of-plane fiber orientation distributions. Here, 90° indicates rotational (preferential) and planar directions in the in-plane and out-of-plane fiber orientation distributions, respectively. Videos of the 3D rendered images acquired by Bruker microCT® CTvox 3.2.0 are given in the supplementary information. Here, the CTvox, a 3D visualization software by Bruker, Belgium, has been used to reconstruct the data obtained from an X-ray microCT scan.

$$r_{el} = 1 + \frac{(\pi + 4V_f\psi)k_j^2}{4I} \quad (3)$$

$$\text{where } \psi = \int_0^\pi d\beta \int_0^\pi d\phi \Omega(\beta, \phi) J(\beta, \phi) K(\beta, \phi) \sin\beta;$$

$$K(\beta, \phi) = \int_0^\pi d\zeta \int_0^\pi d\gamma \Omega(\gamma, \zeta) \frac{\sin\gamma}{\sin\chi(\beta, \phi, \gamma, \zeta)};$$

$$\cos\chi = \cos\beta\cos\gamma + \sin\beta\sin\gamma\cos(\phi - \zeta);$$

$$k_j = \int_0^\pi d\phi \int_0^\pi |\sin\beta\cos\beta|\Omega(\beta, \phi)d\beta$$

where V_f is the fiber volume fraction.

Roughness is a key parameter in maneuvering the wettability of a surface, especially when $r > 1$; then, hydrophilicity or hydrophobicity of the surface gets amplified depending upon the inherent nature of the solid [30]. A rough surface with an appropriate combination of texture and surface energy may not allow the liquid to penetrate into these textures [31]. Thus, a liquid droplet beads-up to form a composite of a solid-liquid-air interface by trapping the air pockets inside the surface textures, and the liquid wets only a fraction of the solid surface. In this direction, the pioneering work of Cassie-Baxter [3] is noteworthy in predicting the apparent contact angle of a composite interface (θ_{CB}^*), as shown in the following equation.

$$\cos\theta_{CB}^* = f_1 \cos\theta_Y - f_2 \quad (4)$$

where f_1, f_2 are the area fractions of the solid/liquid and liquid/air interfaces, respectively.

Similar to the theoretical approach used for predicting r_{el} , the f_1 and f_2 can also be related to the fiber and structural parameters of an electrospun mat, as shown below [28].

$$f_1 = n(\pi - \theta_Y) \quad (5)$$

$$f_2 = 1 - n\sin\theta_Y \quad (6)$$

$$n = \frac{8V_f IF}{\pi + 4V_f\psi} \quad (7)$$

where $F = \int_0^\pi d\beta \int_0^\pi d\phi \Omega(\beta, \phi) K(\beta, \phi) \sin\beta$ and $f_1 + f_2 \geq 1$

One of the ways to identify the onset of the metastable CB state is by obeying equations (2) and (4) simultaneously [12]. Thus, the threshold contact angle (θ') between the two wetting regimes is obtained by equating θ_w^* and θ_{CB}^* in equations (2) and (4), respectively,

$$\cos\theta' = \frac{-f_2}{r - f_1} \quad (8)$$

The stable CB state would be favored when θ_Y is larger than θ' [12]. Herminghaus [32] argued that the metastable state can still be achieved in a substrate with finite hydrophilic characteristics provided that the surface roughness is present in the form of 'overhangs' that allows pinning of the three-phase contact line (TCL) [33]. In such cases, the roughness profile is not a single-valued function, and dual- or multi-scalar roughness can provide an equilibrium position even for hydrophilic substrates [34]. Given the fact that polystyrene is a weakly hydrophilic polymer ($\theta_Y = 83^\circ$), the dual-scale roughness of the electrospun mat and that of the constituent fibers are poised to alter the hydrophilic characteristics. In this scenario, the liquid droplet is suspended on the fibers, as the investigated electrospun mats possess high bulk porosity (see Table S1). Further, the pinning of a TCL occurs due to the overall roughness created by hydrophilic fibers, leading to the metastable [35] or so-called modified 'Cassie-Baxter' state. The effective contact angle on the rough surface is determined by a small displacement of the contact line (dx), which implies a change in surface energy (dE) [36,37],

$$\frac{dE}{dx} = -\cos(\pi - \theta_{CW}^*)\gamma_{LA} + f_2\gamma_{LA} + f_1 r_f r_{el}(\gamma_{SL} - \gamma_{SA}) \quad (9)$$

where θ_{CW}^* is the apparent contact angle in the modified CB state, r_f is the fiber roughness, γ is the surface tension or energy per unit area, and the subscripts, SL , SA , and LA , represent the solid-liquid, solid-air, and liquid-air, respectively.

Using Young's equation, i.e., $\gamma_{LA}\cos\theta_Y = \gamma_{SA} - \gamma_{SL}$ and minimizing the energy, i.e. $\frac{dE}{dx} = 0$, would modify the equation (9) as,

$$\cos\theta_{CW}^* = f_1 r_f r_{el} \cos\theta_Y - f_2 \quad (10)$$

In equation (10), the θ_{CW}^* can be predicted using the fiber and structural parameters of polystyrene-based electrospun mat except for the fact that r_f is unknown. To compute r_f , the wrinkled morphology of the constituent polystyrene fibers can be hypothesized as folds applied in the form of the sinusoidal pattern [38] and subsequently rolled-up preferentially to form the fiber. These simple micro-wrinkled features allowed us to utilize the roughness factor of an idealized sinusoidal surface [39,40], as shown below.

$$r_f = \frac{4\pi A}{\lambda\rho^2} \int_0^\rho \left\{ \frac{\lambda^2 x^2}{4\pi^2 A^2} + x^2 \sin^2 \frac{2\pi x}{\lambda} \right\}^{\frac{1}{2}} dx \quad (11)$$

where $\rho (= R\sin\theta_Y)$ is the radius of the projected liquid drop on the surface [41], $R \left(= \left[\frac{3V}{\pi(1-\cos\theta_Y)^2(2+\cos\theta_Y)} \right]^{\frac{1}{3}} \right)$ is the radius of the sphere that forms a liquid drop [41], V is the volume of the liquid drop, A and λ are the amplitude and wavelength of the sine wave, respectively.

Combining equations (3), (5) - (7), (10), and (11) would predict the apparent contact angles in the static and dynamic modes. In equation (10), the apparent advancing contact (θ_{adv}^*) and receding contact angles (θ_{rec}^*) have been predicted by replacing θ_Y with the corresponding advancing (θ_{adv}) and receding (θ_{rec}) contact angles on the smooth surface, respectively. It should be noted that the equation (10) is useful for predicting the apparent contact angle in the modified CB state, specifically for the materials with a low-level of roughness. The Wenzel equation fails for surfaces with high-level roughness as it leads to the magnitude of cosines that goes beyond the bounds of -1 and $+1$ [39].

Roughness is pivotal in creating a large number of metastable configurations, and each of them is separated by an energy barrier [39]. These multiple free energy barriers are instrumental in avoiding the presumable Wenzel regime. As aforementioned, the roughness in an electrospun mat is induced by the surface morphology of the fibers and the protuberances created by fiber-fiber contacts. Specifically, wrinkling on the fiber surface imparts the first level of hierarchical roughness that can potentially assist in the formation of a metastable state. The underlying mechanism of the surface wrinkling in polystyrene-based electrospun mats is plausibly an outcome of the mismatch between the shell and the core deformations during solvent evaporation [14]. According to Johnson and Detre [39], the externally imparted energy applied in the form of vibrations, pressures, etc., should be lower than the height of the energy barrier for attaining the metastable state on the sinusoidal surface. As expected, the TCL would pin at the highest energy barrier till the advancing drop moves the contact line beyond the sticking point, and subsequently, the fluid enters the valley of the surface [40].

The presence of roughness in the form of a sinusoidal surface causes the equilibrium contact angle (θ_Y) to be less or greater than the apparent contact angle (θ^*) [42]. This depends upon whether the gradient of the solid at the line of contact is positioned in the same or the opposite direction to the liquid surface. For the metastable state, the observed macroscopic contact angle on the sinusoidal fiber surface is presumed to be $\theta^* (= \theta_Y + \alpha)$, where $\alpha \{ = \tan^{-1}[(2\pi A/\lambda)(\sin 2\pi x/\lambda)] \}$ is the slope angle of the solid-liquid surface [39,42]. Here, α is minimum (α_{min}) and

maximum (α_{\max}) when $\sin 2\pi x/\lambda = -1$ and $\sin 2\pi x/\lambda = 1$, respectively. Accordingly, these geometrical constraints would provide the minimum and maximum apparent contact angles as $\theta_{\min}^* = \theta_Y - \alpha_{\max}$ and $\theta_{\max}^* = \theta_Y + \alpha_{\max}$, respectively [40]. In this research work, the calculated values of θ_{\min}^* and θ_{\max}^* are 39° and 128° , respectively, and these values represent the absolute limits to receding and advancing contact angles [42]. Interestingly, the height of the energy barrier attains zero as θ^* approaches θ_{\min}^* and θ_{\max}^* but such magnitudes of θ^* are unlikely to be detected realistically on a hydrophilic surface [39,40].

A commonly used rule of thumb suggests that the height of the energy barrier scales with the amplitude (A) and the slope angle (α) [39,40]. Higher magnitudes of amplitude are inevitably beneficial for attaining a composite surface, but it may still be energetically preferable for the liquid to penetrate in the valleys. This suggests that the wetting of the sinusoidal surface is bound to take place in the region defined by the TCL (see Fig. 4). Accordingly, the asperity present on the fiber surface that comes in direct contact with the TCL is expected to be wetted. Based upon the methodology employed by Bormashenko et al. [43], the energy barrier required to fill an asperity (E_{trans}) can be approximately expressed as $-2\pi R\langle A \rangle \gamma_{LA} \cos \theta_Y$, where $\langle \rangle$ represents the mean value. A $10 \mu\text{L}$ drop lying on a given asperity ($\langle A \rangle = 26 \text{ nm}$, and $\langle \lambda \rangle = 168 \text{ nm}$) exhibits the following parameters, $R = 1.79 \text{ mm}$, $\gamma = 0.072 \text{ J/m}^2$, $\theta_Y = 83^\circ$, thus the magnitude of energy required to wet this asperity is $2.56 \times 10^{-3} \text{ nJ}$. The energy barrier required to wet a weakly hydrophilic sinusoidal surface is several orders of magnitude lower in comparison to a moderately hydrophobic post [43,44]. Thus, the sinusoidal surface that directly comes in contact with the TCL is expected to be wetted fully, as illustrated in Fig. 4.

In the past, the re-entrant structure of the electrospun mat has successfully led to the development of superhydrophobic characteristics from hydrophilic fibers [8,45]. The re-entrant structure ensures a robust metastable state of the liquid, and the wrinkles present on the fiber surface can create a 'doubly re-entrant' structure. Analogous to the microscale posts with nanoscale vertical overhangs [46], the liquid can be suspended on the wrinkled fibers with the aid of surface tension only. Fig. 4 depicts the movement of the drop edge present on the top of the curved fiber surface. Here, when the drop shifts from position A to B, the resultant vector of the surface tension acts to move the drop back to A, leading to pinning of the drop [39] (see Fig. 4). On the other hand, when the drop shifts from C to D, the resultant acts in the direction of D, leading to the spreading of the drop. This competition of resultant vectors of surface tension can effectively lead to the composite wetting state of the wrinkled surfaces, which are not in direct contact with the TCL (see Fig. 4). The metastability of the composite wetting state is also

enhanced due to the presence of stochastically aligned fibers that trap the air in the highly porous structure of the electrospun mat.

High bulk porosity of an electrospun mat is a crucial factor in enhancing the hydrophobicity, though it also corresponds to the sagging tendency of the TCL, which affects the robustness of the metastable state [28,47]. To gain deeper insight into the robustness of the metastable state of the electrospun samples, we revisited the dimensionless pressure difference across the liquid – vapor interface (P^*), using porosity and fiber orientation distribution as key material parameters in the following

equation, i.e. $P^* = \frac{2\eta}{F} \left[\frac{\sqrt{1-n^2 \sin^2 \theta_Y}}{n \cos \theta_Y + \sqrt{1-n^2 \sin^2 \theta_Y}} \right]$ [28]. The significance of P^*

implies a wet-through resistance of the meniscus possessing maximum curvature before touching the substrate. In other words, the higher magnitude of P^* suggests more robustness of the metastable state of the liquid on the substrate. Table S1 shows that the magnitude of P^* is reasonably higher for ES-B than ES-A. As aforementioned, ES-B possesses a preferential structure that provides sufficient hindrance to the movement of the TCL. It is plausible that the formation of a new interface of solid–liquid occurs continuously in a random structure.

In general, a trade-off between the fiber alignments, topological aspects of the wrinkled fiber surface, and overall bulk porosities has resulted in similar magnitudes of apparent (static) contact angles in ES-A and ES-B (see Table S1). Similarly, the advancing contact angles of the electrospun mats were nearly found to be the same, as shown in Table S1. However, the receding contact angles (θ_{rec}^*) of ES-A and ES-B were significantly different. Thus, the contact angle hysteresis (CAH) was much higher ($\sim 57^\circ$) in ES-A than that of ES-B ($\sim 34^\circ$). Such results clearly indicate that the orientation of the fibers primarily influences the dewetting properties (θ_{rec}^* and CAH) of the surface rather than the static and advancing contact angles. In this study, the preferential orientation of fibers in ES-B is apparently insufficient to distort the shape of the water drops from that of a spherical cap (see Figure S3). Such distortion has been observed elsewhere with more highly aligned fibers [48]. There are other factors that also affect the elongation of the water drop, i.e., fiber diameter, porosity, type of polymer, fiber morphology, and volume of liquid. Nevertheless, an automated in-house developed instrument has been used for the measurement of roll-off angles to confirm the metastable CB state of the water droplet, as shown in Figure S4. Similar to the observations made by Varagnolo et al. [48], the tilting of the electrospun samples causes the movement of the front side of the TCL and then pinned again while it is being turned upside-down, as shown in Fig. 5. However, the rear side of the TCL remains pinned on the surface of the electrospun mats. The evolution of the droplet profile during the roll-off measurement reduced the contact angle nearly by 30°

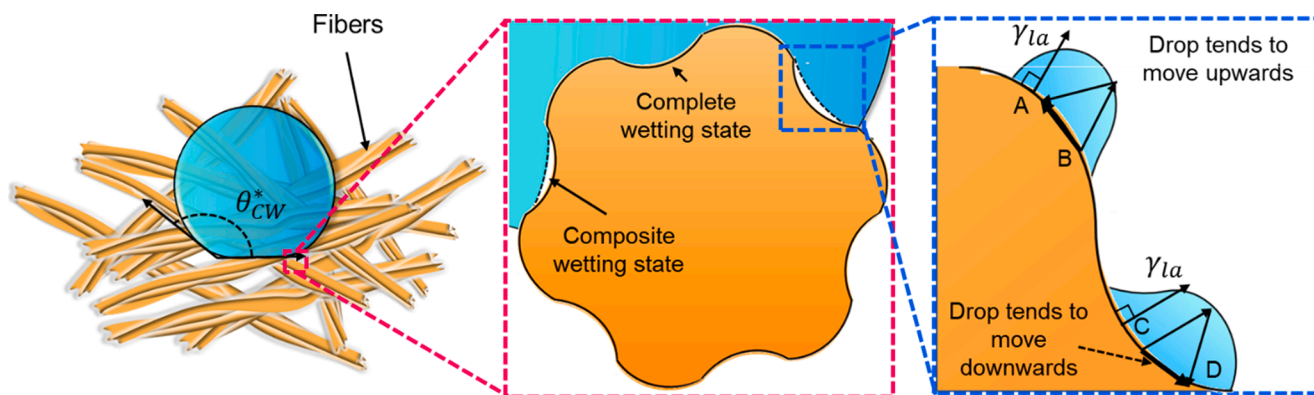


Fig. 4. Schematic depicting the modified CB state of the liquid drop on the surface of the electrospun mat. The first magnified image illustrates the complete and composite-wetting states of the wrinkled fiber surface hypothesized as sinusoidal folds. Here, the complete wetting represents the Wenzel regime formed on the sinusoidal fold that comes in direct contact with TCL. A composite wetting state is formed as a result of the competition between the resultant surface tension vectors depending upon the region of interfacial contact of the solid–liquid phases on a radially aligned sinusoidal fold. These minute details are pictorially highlighted in the magnified portion of the fiber.

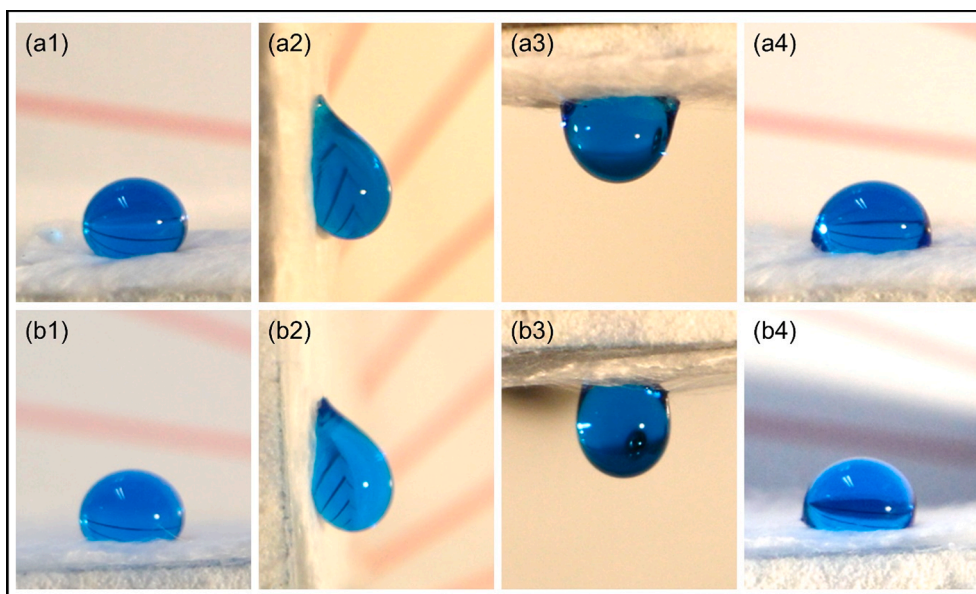


Fig. 5. Water droplet (demineralized water is tinted with methylene blue) profiles depicted on the surface of ES-A (a1-a4) and ES-B (b1-b4). Here, (a1, b1) show the initial state of the water drop, (a2, b2) exemplify the water drop in the vertical direction, (a3, b3) illustrate the water drop in the upside down state, and (a4, b4) demonstrate the final state of the water drop after tilting back to the horizontal position.

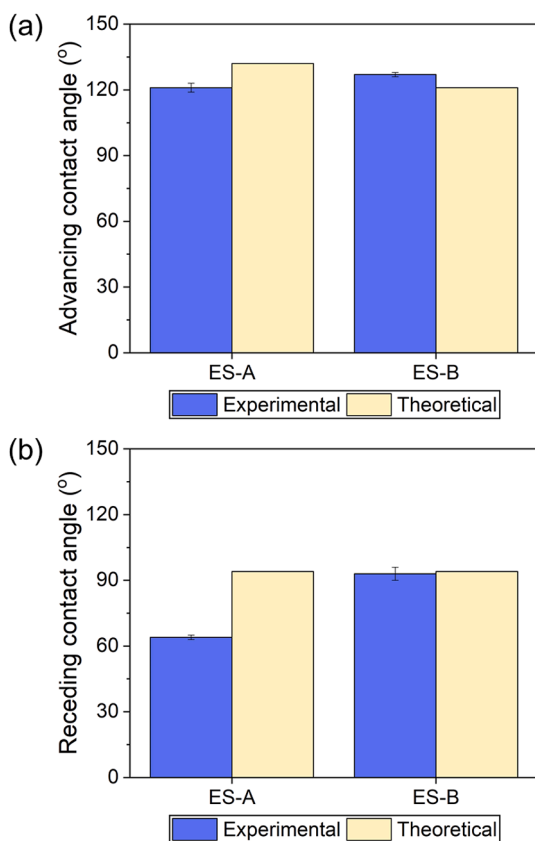


Fig. 6. Comparison between the theoretical and experimental values of apparent (a) advancing and (b) receding contact angles of ES-A and ES-B. Here, the ES-A and ES-B samples correspond to the preferentially and randomly aligned electrospun mats, respectively.

and 20° for ES-A and ES-B, respectively. This implies that higher infiltration and strong adhesion of water with the electrospun mats occur, confirming the metastable CB state [48].

A comparison has also been made between the theoretical and

experimental values of advancing and receding contact angles, as illustrated in Fig. 6. In general, a reasonable agreement has been observed between the theory and experiments. Here, the theoretical apparent advancing contact angle (θ_{adv}^*) and receding contact angle (θ_{rec}^*) have been predicted by replacing the θ_{CW}^* in the equation (10). Also, the advancing and receding contact angles of water on a smooth flat polystyrene surface were considered to be 90° and 70° , respectively [49]. For predicting the value of θ_{rec}^* , the maximum magnitude of area fraction of solid ($f_1=1$) has been considered by employing the methodology of Choi et al. [31] for a grid type of structure (referred to as ‘inverse hoodoo’ in ref. [31]). This structure is similar to the characteristics of electrospun mats, where the air pockets (or pores) at the surface are discontinuous and separated by constituent fibers. Therefore, the TCL recedes locally on homogenous solid, and accordingly, the local area solid fraction of unity has been considered for computing the receding contact angles. In the case of electrospun mats, it is extremely challenging to determine the local area fractions as they depend upon the local fiber volume fractions, wrinkle fiber topology, and locally arranged fibers. Therefore, the local area fractions may vary largely, specifically in the case of ES-A, in which the fibers are randomly aligned. Plausibly, the large variation in local area fractions has led to the greater differences between the theoretical and experimental values of advancing and receding contact angles in ES-A. On the other hand, the ES-B is a nonwoven mat that comprises relatively aligned fibrous structure leading to lower differences between the local and global area fractions. The detailed calculation procedure of apparent advancing and receding contact angles of the electrospun mat has been provided in Figure S5. Nevertheless, these theoretical results demonstrated that predictive modeling is sufficiently robust and has encapsulated a key set of fiber and structural parameters.

It should be noted that the predictive modeling cautiously considered the uniform geometry of the fibers, but such ubiquitous nature of regular fibers can sometimes be questionable. Polystyrene being a versatile polymer, a variety of arbitrary geometries can easily be created, ranging from hollow [50], core-shell [51], to bead-on-string [52] using the electrospinning technique. Beaded fibers are well-known to exist in the electrospun mats due to the dominance of the surface tension that effectively allows the formation of droplets via the Rayleigh instability effect [53]. In the past, the hydrophilic poly(caprolactone) beaded fibers demonstrated the metastable hydrophobic state [53]. However, the

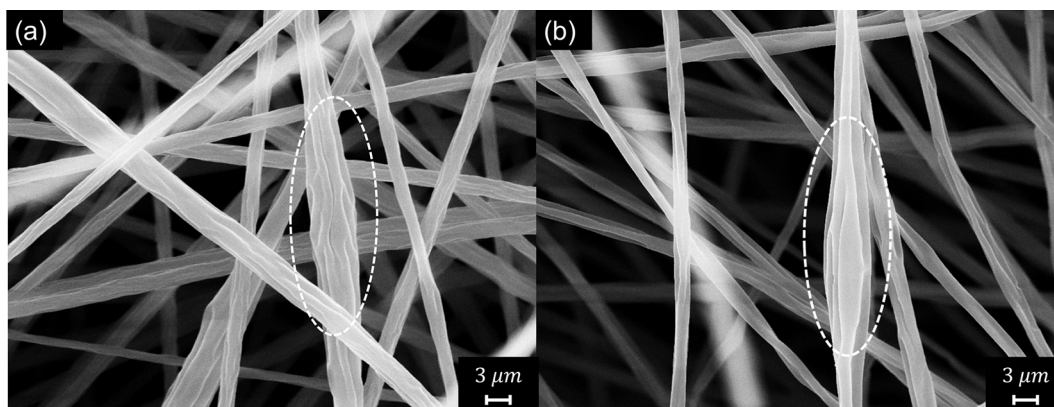


Fig. 7. SEM images of (a) ES-A and (b) ES-B depicting the sporadic presence of elongated beads.

higher density of smaller beads tended to enhance the contact angle more than a lower density of larger beads. In this research work, the elongated beads approximating the prolate spheroid geometry have also been sporadically observed. Fig. 7 shows the presence of such elongated beads in the electrospun mats.

These elongated beads possess moderate to high levels of the roughness of the fibers, and a sufficient proportion of them ensures enhancing the metastable hydrophobic state.

4. Conclusions

In this research work, the metastable state of the liquid in contact with the polystyrene-based electrospun mats comprising wrinkled surface topography has been investigated via theoretical modeling and a systematic set of experiments. Though the inherent nature of the electrospun fibers was weakly hydrophilic, the mats displayed moderate hydrophobic characteristics. These experimental observations have led to the development of an analytical model of apparent contact angle based on the modified Cassie-Baxter state. This predictive model is the first of its kind to consider dual-scale roughness due to wrinkled fiber topography and fiber-fiber contacts as a key input. Specifically, the wrinkled morphology of the polystyrene fibers has been hypothesized as folds applied in the form of a sinusoidal pattern for computing the Wenzel roughness factor. Further, the energy barrier required to wet a weakly hydrophilic sinusoidal fold was found to be extremely low in magnitude so that the fully wetted state of the wrinkled surface that directly comes in contact with the TCL is manifested. A trade-off between the resultant vectors of surface tension can effectively lead to the composite wetting state over the wrinkled surfaces. Further, the 'doubly re-entrant' structure of the wrinkled fiber surface ensured a reasonable robust metastable state of the liquid. The robustness of the metastable state of the electrospun mats was quantified via the dimensionless pressure difference across the liquid – vapor interface. Further, the X-ray microCT analysis has been successfully employed to gain insights into these fiber and structural parameters. A reasonable agreement was observed between the theoretical and experimental magnitudes of the apparent contact angles in the advancing and receding modes based on the modified CB state. Intriguingly, the static and advancing contact angles in randomly and aligned electrospun mats with water drops were observed to be the same, but the receding contact angles were considerably different.

CRediT authorship contribution statement

Amit Rawal: Conceptualization, Methodology, Writing - review & editing, Funding acquisition. **Siddharth Shukla:** Formal analysis, Methodology, Software, Visualization. **Sumit Sharma:** Methodology, Software, Validation, Visualization. **Danvendra Singh:** Methodology,

Software, Validation. **Yi-Min Lin:** Investigation, Writing - original draft. **Junli Hao:** Investigation. **Gregory C. Rutledge:** Conceptualization, Methodology, Writing - review & editing, Funding acquisition. **Lívía Vásárhelyi:** Investigation, Software, Visualization. **Kozma Gábor:** Investigation, Software, Visualization. **Akos Kukovecz:** Conceptualization, Methodology, Funding acquisition. **László Janovák:** Investigation, Software, Funding acquisition, Writing - review & editing.

Declaration of Competing Interest

None

Acknowledgement

AR acknowledges the financial support from the United States–India Educational Foundation (USIEF) for his visit to MIT, Cambridge, under the Fulbright-Nehru Academic and Professional Excellence Fellowship program. LJ also acknowledges the UNKP-20-5 New National Excellence Program of the Ministry for Innovation and Technology from the source of the National Research, Development and Innovation Fund and by the János Bolyai Research Scholarship of the Hungarian Academy of Sciences. This work has also been financially supported by Indo-Hungarian joint research project no. INT/HUN/P-18/2017 (NKFIH 2017-2.3.7-TÉT-IN-2017-00008). The support provided by the Hungarian National Innovation Research and Development Office for the acquisition of the microCT instrument through the GINOP-2.3.3-15-2016-00010 project is acknowledged. We are also indebted to Dr. P.V. Kameswara Rao, for his valuable suggestions with regard to the AFM analysis.

Appendix A. Supplementary data

Supplementary data to this article can be found online at <https://doi.org/10.1016/j.apsusc.2021.149147>.

References

- [1] T.-S. Wong, T. Sun, L. Feng, J. Aizenberg, Interfacial materials with special wettability, *MRS Bull.* 38 (5) (2013) 366–371.
- [2] R.N. Wenzel, Resistance of solid surfaces to wetting by water, *Ind. Eng. Chem.* 28 (8) (1936) 988–994.
- [3] A.B.D. Cassie, S. Baxter, Wettability of porous surfaces, *Trans. Faraday Soc.* 40 (1944) 546–551.
- [4] S.T. Yohe, J.D. Freedman, E.J. Falde, Y.L. Colson, M.W. Grinstaff, A mechanistic study of wetting superhydrophobic porous 3D meshes, *Adv. Funct. Mater.* 23 (29) (2013) 3628–3637.
- [5] M. Ma, M. Gupta, Z. Li, L. Zhai, K.K. Gleason, R.E. Cohen, M.F. Rubner, G. C. Rutledge, Decorated electrospun fibers exhibiting superhydrophobicity, *Adv. Mater.* 19 (2) (2007) 255–259.
- [6] Y. Shang, Y. Si, A. Raza, L. Yang, X. Mao, B. Ding, J. Yu, An in situ polymerization approach for the synthesis of superhydrophobic and superoleophilic nanofibrous membranes for oil–water separation, *Nanoscale.* 4 (24) (2012) 7847.

- [7] U. Stachewicz, R.J. Bailey, H. Zhang, C.A. Stone, C.R. Willis, A.H. Barber, Wetting hierarchy in oleophobic 3D electrospun nanofiber networks, *ACS Appl. Mater. Interfaces*. 7 (30) (2015) 16645–16652.
- [8] A. Tuteja, W. Choi, M. Ma, J.M. Mabry, S.A. Mazzella, G.C. Rutledge, G. H. McKinley, R.E. Cohen, Designing superoleophobic surfaces, *Science*. 318 (5856) (2007) 1618–1622.
- [9] A. Marmur, The lotus effect: superhydrophobicity and metastability, *Langmuir*. 20 (2004) 3517–3519.
- [10] Y.-T. Cheng, D.E. Rodak, Is the lotus leaf superhydrophobic? *Appl. Phys. Lett.* 86 (14) (2005) 144101.
- [11] J. Bico, C. Marzolin, D. Quéré, Pearl drops, *EPL Europhys. Lett.* 47 (2) (1999) 220–226.
- [12] A. Lafuma, D. Quéré, Superhydrophobic states, *Nat. Mater.* 2 (7) (2003) 457–460.
- [13] C.-L. Pai, M.C. Boyce, G.C. Rutledge, Morphology of porous and wrinkled fibers of polystyrene electrospun from dimethylformamide, *Macromolecules*. 42 (6) (2009) 2102–2114.
- [14] L. Wang, C.-L. Pai, M.C. Boyce, G.C. Rutledge, Wrinkled surface topographies of electrospun polymer fibers, *Appl. Phys. Lett.* 94 (2009), 151916.
- [15] J. Lin, B. Ding, J. Yu, Direct fabrication of highly nanoporous polystyrene fibers via electrospinning, *ACS Appl. Mater. Interfaces*. 2 (2) (2010) 521–528.
- [16] A.K. Haridas, C.S. Sharma, V. Sritharan, T.N. Rao, Fabrication and surface functionalization of electrospun polystyrene submicron fibers with controllable surface roughness, *RSC Adv.* 4 (24) (2014) 12188.
- [17] Z.J. Krysiak, M.Z. Gawlik, J. Knapczyk-Korczak, \Lukasz Kaniuk, U. Stachewicz, Hierarchical Composite Meshes of Electrospun PS Microfibers with PA6 Nanofibers for Regenerative Medicine, *Materials*. 13 (2020) 1974.
- [18] Joanna Knapczyk-Korczak, Daniel P. Ura, Marcin Gajek, Mateusz M. Marzec, Katarzyna Berent, Andrzej Bernasik, John P. Chiverton, Urszula Stachewicz, Fiber-based composite meshes with controlled mechanical and wetting properties for water harvesting, *ACS Appl. Mater. Interfaces*. 12 (1) (2020) 1665–1676.
- [19] Gerd Gaiselmann, Christian Tötze, Ingo Manke, Werner Lehnert, Volker Schmidt, 3D microstructure modeling of compressed fiber-based materials, *J. Power Sources*. 257 (2014) 52–64.
- [20] S. Shukla, V. Kumar, P.V. Kameswara Rao, S. Sharma, D. Sebök, I. Szenti, A. Rawal, A. Kukovec, Probing the three-dimensional porous and tortuous nature of absorptive glass mat (AGM) separators, *J. Energy Storage*. 27 (2020), 101003.
- [21] D. Nečas, P. Klapetek, Gwyddion: an open-source software for SPM data analysis, *Open Phys.* 10 (2012) 181–188.
- [22] Looh Tchuin Choong, Peng Yi, Gregory C. Rutledge, Three-dimensional imaging of electrospun fiber mats using confocal laser scanning microscopy and digital image analysis, *J. Mater. Sci.* 50 (8) (2015) 3014–3030.
- [23] Takashi Komori, Kunio Makishima, Numbers of fiber-to-fiber contacts in general fiber assemblies, *Text. Res. J.* 47 (1) (1977) 13–17.
- [24] Vijay Kumar, Amit Rawal, Tuning the electrical percolation threshold of polymer nanocomposites with rod-like nanofillers, *Polymer*. 97 (2016) 295–299.
- [25] Tomas Rosén, Christophe Brouzet, Stephan V. Roth, Fredrik Lundell, L. Daniel Söderberg, Three-Dimensional Orientation of Nanofibrils in Axiially Symmetric Systems Using Small-Angle X-ray Scattering, *J. Phys. Chem. C*. 122 (12) (2018) 6889–6899.
- [26] R.D. Hazlett, On surface roughness effects in wetting phenomena, *J. Adhes. Sci. Technol.* 6 (6) (1992) 625–633.
- [27] Robert N. Wenzel, Surface roughness and contact angle, *J. Phys. Chem.* 53 (9) (1949) 1466–1467.
- [28] Amit Rawal, Design parameters for a robust superhydrophobic electrospun nonwoven mat, *Langmuir*. 28 (6) (2012) 3285–3289.
- [29] Amit Rawal, Sumit Sharma, Vijay Kumar, Harshvardhan Saraswat, Designing superhydrophobic disordered arrays of fibers with hierarchical roughness and low-surface-energy, *Appl. Surf. Sci.* 389 (2016) 469–476.
- [30] David Quéré, Wetting and roughness, *Annu Rev Mater Res.* 38 (1) (2008) 71–99.
- [31] Wonjae Choi, Anish Tuteja, Joseph M. Mabry, Robert E. Cohen, Gareth H. McKinley, A modified Cassie-Baxter relationship to explain contact angle hysteresis and anisotropy on non-wetting textured surfaces, *J. Colloid Interface Sci.* 339 (1) (2009) 208–216.
- [32] S Herminghaus, Roughness-induced non-wetting, *EPL Europhys. Lett.* 52 (2) (2000) 165–170.
- [33] José Bico, Uwe Thiele, David Quéré, Wetting of textured surfaces, *Colloids Surf. Physicochem. Eng. Asp.* 206 (1-3) (2002) 41–46.
- [34] G. Carbone, L. Mangialardi, Hydrophobic properties of a wavy rough substrate, *Eur. Phys. J. E.* 16 (1) (2005) 67–76.
- [35] Jianlin Liu, Yue Mei, Re Xia, A new wetting mechanism based upon triple contact line pinning, *Langmuir*. 27 (1) (2011) 196–200.
- [36] Tae-Gon Cha, Jin Woo Yi, Myoung-Woon Moon, Kwang-Ryeol Lee, Ho-Young Kim, Nanoscale patterning of microtextured surfaces to control superhydrophobic robustness, *Langmuir*. 26 (11) (2010) 8319–8326.
- [37] Krisztina Nagy, Krishn Gopal Rajput, Ildikó Y. Tóth, P.V. Kameswara Rao, Sumit Sharma, Vijay Kumar, Amit Rawal, Akos Kukovec, Self-similar arrays of carbon nanotubes and nonwoven fibers with tunable surface wettability, *Mater. Lett.* 228 (2018) 133–136.
- [38] Peter Cendula, Suwit Kiravittaya, Ingolf Mönch, Joachim Schumann, Oliver G. Schmidt, Directional roll-up of nanomembranes mediated by wrinkling, *Nano Lett.* 11 (1) (2011) 236–240.
- [39] R.E. Johnson Jr, R.H. Dettre, Contact angle hysteresis: I. Study of an idealized rough surface, in, *ACS Publications* (1964).
- [40] Jun Young Chung, Jeffrey P. Youngblood, Christopher M. Stafford, Anisotropic wetting on tunable micro-wrinkled surfaces, *Soft Matter*. 3 (9) (2007) 1163.
- [41] C. Huh, S.G. Mason, Effects of surface roughness on wetting (theoretical), *J. Colloid Interface Sci.* 60 (1) (1977) 11–38.
- [42] R. Shuttleworth, G.L.J. Bailey, The spreading of a liquid over a rough solid, *Discuss. Faraday Soc.* 3 (1948) 16–22.
- [43] E. Bormashenko, Comment on water droplet motion control on superhydrophobic surfaces: exploiting the Wenzel-to-Cassie transition, *Langmuir*. 27 (2011) 12769–12770.
- [44] Laura Barbieri, Estelle Wagner, Patrik Hoffmann, Water wetting transition parameters of perfluorinated substrates with periodically distributed flat-top microscale obstacles, *Langmuir*. 23 (4) (2007) 1723–1734.
- [45] Minglin Ma, Randal M. Hill, Gregory C. Rutledge, A review of recent results on superhydrophobic materials based on micro-and nanofibers, *J. Adhes. Sci. Technol.* 22 (15) (2008) 1799–1817.
- [46] Tingyi “Leo” Liu, Chang-Jin “CJ” Kim, Turning a surface superrepellent even to completely wetting liquids, *Science*. 346 (6213) (2014) 1096–1100.
- [47] Jiann Shieh, Fu Ju Hou, Yan Chen Chen, Hung Min Chen, Shun Po Yang, Chao Chia Cheng, Hsuen Li Chen, Robust airlike superhydrophobic surfaces, *Adv. Mater.* 22 (5) (2010) 597–601.
- [48] S. Varagnolo, F. Raccanello, M. Pierno, G. Mistura, M. Moffa, L. Persano, D. Pisignano, Highly sticky surfaces made by electrospun polymer nanofibers, *RSC Adv.* 7 (10) (2017) 5836–5842.
- [49] O.I. Vinogradova, G.E. Yakubov, H.-J. Butt, Forces between polystyrene surfaces in water–electrolyte solutions: Long-range attraction of two types? *J. Chem. Phys.* 114 (2001) 8124–8131.
- [50] K.H. Lee, H.Y. Kim, H.J. Bang, Y.H. Jung, S.G. Lee, The change of bead morphology formed on electrospun polystyrene fibers, *Polymer*. 44 (14) (2003) 4029–4034.
- [51] Keith M. Forward, Alexander Flores, Gregory C. Rutledge, Production of core/shell fibers by electrospinning from a free surface, *Chem. Eng. Sci.* 104 (2013) 250–259.
- [52] Jianfen Zheng, Aihua He, Junxing Li, Jian Xu, Charles C. Han, Studies on the controlled morphology and wettability of polystyrene surfaces by electrospinning or electrospaying, *Polymer*. 47 (20) (2006) 7095–7102.
- [53] Minglin Ma, Yu Mao, Malancha Gupta, Karen K. Gleason, Gregory C. Rutledge, Superhydrophobic fabrics produced by electrospinning and chemical vapor deposition, *Macromolecules*. 38 (23) (2005) 9742–9748.